Semi-Analytical Solution to Heat-Transfer Problems Using Fourier Transform Technique, Radial Basis Functions and the Method of Fundamental Solutions

E.V. Glushkov, N.V. Glushkova

Kuban State University, Krasnodar, 350040, Russia

E-mail: evg@math.kubsu.ru

C.S. Chen

Department of Mathematics

University of Southern Mississippi

Hattiesburg, MS 39406, U.S.A.

E-mail: cs.chen@usm.edu

March 9, 2007

Abbreviated title for the running head:

Semi-Analytical Solution to Heat-Transfer Problems

Abstract

An analytically based approach for solving a transient heat-transfer equation in a bounded 2D domain is proposed. The major features of the method are: time-Fourier transformation of the problem, analytical derivation of an elementary particular solution for a localized radial basis δ-like source using the space-Fourier transform, expansion of the total particular solution in terms of those elementary particular solutions, approximation of the homogeneous solution using the method of fundamental solution, inversion into the time domain using FFT. The prime distinction of this scheme from the closest analogues lies in the particular solution construction.

1 Introduction

Numerical solution of heat transfer problems have been well established over the past four decades. It is well-known that through various types of reduction techniques a given heat transfer problem is normally converted to a series of elliptical equations which can be solved by the traditional numerical methods such as finite element, finite difference, and boundary element methods. To remove the time-dependent variable, the following approaches are widely adopted: (i) Laplace transform method [1, 2, 3, 4] (ii) finite difference time stepping scheme [5, 6, 7, 8, 9] (iii) time-space separation method [10, 11]. Since the numerical inversion of Laplace transform is an ill-posed problem, small truncation errors are magnified in the numerical inversion process. As a result, the accuracy of the final result is greatly affected. For time stepping scheme, small time step is required to achieve a reasonable accuracy. The numerical computation is not cost effective. Furthermore, when the time step is too small, it may also cause other difficulties in numerical computation [6]. For time-space separation scheme, there are difficulties when the forcing term is a function of time [11]. A common feature of the first two schemes is that a heat transfer problem is reduced to a series of nonhomogeneous modified Helmholtz equations. Notably, in the boundary element literature, dual reciprocity method [3] has been employed to solve these equations. Chen et al [4] applied the method of particular solution and the method of fundamental solutions (MFS) [12, 13, 14] to form a boundary meshless approach with improving results and efficiency. The derivation of closed form particular

solution for the nonhomogeneous Helmholtz-type equations [14, 15, 16] is crucial for the success of above mentioned meshless approach. Despite the effectiveness of solving elliptic problems using either the traditional methods or meshless methods, the overall accuracy is heavily depend on the treatment of time-dependent variable which is considered as the bottleneck for solving the heat transfer problems.

It is the purpose of this paper to propose a mesh free method through the use of Fourier transform to remove the time-dependent variable. As a result, the given heat transfer problem is reduced to Helmholtz equation in frequency domain. A boundary-type meshless method is applied to solve Helmholtz equation. Then, the fast Fourier transform is employed to convert the solution in frequency domain to time domain. The detailed numerical procedure is given in the next section. Meanwhile, we would like to emphasize the derivation of a closed form particular solution is also a main focus in this paper. For a given nonhomogeneous linear elliptic equation, if the fundamental solution and particular solution are both available, the problem can be solved effortless. In the boundary element community, the fundamental solutions have been derived for a large class of differential equations. However, the closed form particular solution are much more difficult to obtain due to the uncertainty of nonhomogeneous term (or forcing term). During the past decade, intensive research have been conducted to derive close form approximate particular solutions for Laplacian and Helmholtz-type differential operators [7, 14, 16, 17, 18]. Without the closed form particular solution, the domain integration is normally required. Hence, the domain discretization and singular integration are necessary. In our meshless approach, we try to avoid all these time consuming numerical processes. For that, we propose, in particular, to use expansions in terms of δ-like radial basis functions that already proved high efficiency with elastodynamic problems [19].

The structure of the paper is as follows. In Section 2, we give an outline of the solution procedures. In Section 3, we derive an approximate semi-analytic particular solution for a Helmholtz equation in frequency domain; δ-like radial basis functions have been employed to approximate the forcing term of nonhomogeneous Helmholtz equation. In Section 4, a brief introduction of the method of fundamental solutions is given to solve the homogeneous equation. In Section 5, numerical results in frequency domain of a heat transfer problem are given. In Section 6, numerical results in time domain are obtained

using fast Fourier transform. In Section 7, we draw conclusions and discuss directions for future research.

2 Problem formulation

Let us consider a temperature field $T(\mathbf{x},t)$ in a bounded domain $\Omega \subset R^2$ governed by the heat transfer equation

$$\Delta T\left(\mathbf{x},t\right) = \frac{1}{K}\frac{\partial T\left(\mathbf{x},t\right)}{\partial t} + f\left(\mathbf{x},t\right), \quad \mathbf{x} \in \Omega, \quad 0 \leq t < \infty, \tag{1}$$

where $\mathbf{x} = (x, y)$ is a space point in $2D$, t is time, $K = k/\rho c$ is the thermal diffusivity, k is the thermal conductivity, ρ is the material density, c is the thermal coefficient, and $f(\mathbf{x}, t)$ is a source function. In addition to the heat source f, the field T may be caused by an initial temperature distribution:

$$T(\mathbf{x}, 0) = T_0(\mathbf{x}), \quad \mathbf{x} \in \Omega \tag{2}$$

and by a heat transfer through the boundary $S = \partial\Omega$. Boundary conditions on $S = S_D \cup S_N$, $S_D \cap S_N = \emptyset$ can be both of Dirichlet and Newmann types:

$$T(\mathbf{x}, t) = T_D(\mathbf{x}, t), \quad \mathbf{x} \in S_D, \tag{3}$$

$$\frac{\partial T(\mathbf{x}, t)}{\partial n} = T_N(\mathbf{x}, t), \quad \mathbf{x} \in S_N, \tag{4}$$

where $\mathbf{x} = \mathbf{x}(s) \in S$, s is a parameter of local coordinates along the boundary S, $\mathbf{n}$ is the outward normal to S. Without loss of generality, the action of the sources may be assumed to be limited in time (i.e. there exists t_1 such that $f = T_D = T_N = 0$ for $t \geq t_1$), or they are absent at all ($t_1 = 0$), so that T decays at infinity; i.e.,

$$T(\mathbf{x}, t) \to 0 \quad \text{as} \quad t \to \infty \tag{5}$$

Using the Fourier transform $\mathcal{F}_t$ with respect to the time $t \in [0, \infty)$, we have

$$\hat{T}(\mathbf{x}, \omega) = \mathcal{F}_t[T(\mathbf{x}, t)] = \int_0^\infty T(\mathbf{x}, t) e^{i\omega t} dt, \tag{6}$$

and the time-domain solution $T(\mathbf{x}, t)$ of the Initial Boundary Value Problem (1) - (5) can be expressed via the Fourier-domain solution $\hat{T}(\mathbf{x}, \omega)$ as

$$T(\mathbf{x}, t) = \mathcal{F}_t^{-1}[\hat{T}(\mathbf{x}, \omega)] = \frac{1}{2\pi} \int_{-\infty}^\infty \hat{T}(\mathbf{x}, \omega) e^{-i\omega t} d\omega, \tag{7}$$

where ω is the Fourier spectral parameter or frequency.

Since no poles of the spectral function $\hat{T}$ appear in the upper half-plane $\mathrm{Im}\,\omega > 0$ of the complex plane ω, the integration contour in (7) may be displaced upward from the real axis on some value η; i.e., $\omega = \omega_1 + i\omega_2, -\infty < \omega_1 < \infty$, $\omega_2 = \eta$. Such contour deviation is used to avoid possible singularities on the real axis (in our case in the origin $\omega = 0$). Based on a well-known property $\hat{T}(\mathbf{x}, \omega) = \hat{T}^*(\mathbf{x}, \tilde{\omega})$ ($\tilde{\omega} = -\omega_1 + i\omega_2$, the star denotes complex conjugation), integration in the complex plane ω can be reduced to a ray $0 \le \omega_1 < \infty$ going at a distance η from the real semi-axis

$$T(\mathbf{x}, t) = \frac{1}{\pi}\,\mathrm{Re}\int_0^\infty \hat{T}(\mathbf{x}, \omega)e^{-i\omega t}d\omega_1, \quad \omega = \omega_1 + i\eta, \quad \eta > 0. \tag{8}$$

Fourier transform (6) converts the problem (1) - (5) into the form

$$\Delta\hat{T}(\mathbf{x}, \omega) + \lambda^2\hat{T}(\mathbf{x}, \omega) = \hat{f}(\mathbf{x}, \omega), \quad \mathbf{x} \in \Omega, \tag{9}$$

$$\hat{T}(\mathbf{x}, \omega) = \hat{T}_D(\mathbf{x}, \omega), \quad \mathbf{x} \in S_D, \tag{10}$$

$$\frac{\partial\hat{T}(\mathbf{x}, \omega)}{\partial n} = \hat{T}_N(\mathbf{x}, \omega), \quad \mathbf{x} \in S_N, \tag{11}$$

where

$$\lambda^2 = \frac{i\omega}{K}, \quad \hat{f}(\mathbf{x}, \omega) = -\frac{T_0(x)}{K} + \hat{f}_0(\mathbf{x}, \omega),$$
$$\hat{f}_0 = \mathcal{F}_t[f], \quad \hat{T}_D = \mathcal{F}_t[T_D], \quad \hat{T}_N = \mathcal{F}_t[T_N].$$

In this way, we have converted the heat transfer problem (1) - (5) into Helmholtz equation (9) with boundary condition (10) - (11) which is a steady-state harmonic wave problem except with the complex wave number $\lambda = \lambda_1 + i\lambda_2$, $\lambda_1 = \lambda_2 = \sqrt{\omega/2K}$ instead of a real wave number ($\lambda_2 = 0$, waves in ideal non-absorbing media). Therefore, there is no need to introduce an artificial viscosity $\omega_2 > 0$ as it has been carried out in wave problems in accordance with the principle of limiting absorption. However, the η-shift from the point of singularity $\omega = 0$ in (8) makes sense regarding the calculation of some integrals stated below.

In general, $\hat{T}$ can be obtained as the sum of particular and homogeneous solutions: $\hat{T} = \hat{T}_p + \hat{T}_h$. The particular solution $\hat{T}_p$ satisfies (9), but it does not necessary satisfy the boundary conditions:

$$\Delta\hat{T}_p(\mathbf{x}, \omega) + \lambda^2\hat{T}_p(\mathbf{x}, \omega) = \hat{f}(\mathbf{x}, \omega), \quad \mathbf{x} \in \Omega, \tag{12}$$

while the homogeneous solution satisfies the following homogeneous equation with modified boundary conditions:

$$\Delta\hat{T}_h(\mathbf{x},\omega) + \lambda^2\hat{T}_h(\mathbf{x},\omega) = 0, \quad \mathbf{x} \in \Omega, \tag{13}$$

$$\hat{T}_h(\mathbf{x},\omega) = \hat{T}_D(\mathbf{x},\omega) - \hat{T}_p(\mathbf{x},\omega), \quad \mathbf{x} \in S_D, \tag{14}$$

$$\frac{\partial\hat{T}_h}{\partial n}(\mathbf{x},\omega) = \hat{T}_N(\mathbf{x},\omega) - \frac{\partial T_p}{\partial n}(\mathbf{x},\omega), \quad \mathbf{x} \in S_N. \tag{15}$$

In this paper we propose the following solution procedures for semi-analytical approximation and numerical evaluation of the total field $T(\mathbf{x},t)$:

1. By the Fourier transform $\mathcal{F}_t$, the initial problem (1) - (4) is converted to solving the particular solution in (12) and homogeneous solution in (13) - (15).

2. The right-hand side $\hat{f}$ in (12) is expanded in terms of radial basis functions (RBF) φ_i associated with the nodes $\mathbf{x}_i$ of grid points contained in Ω (Fig. 1):

$$\hat{f}(\mathbf{x},\omega) \approx \sum_{i=1}^{N_i} f_i\varphi_i(\mathbf{x}). \tag{16}$$

   In contrast to the traditional RBF methods [16], φ_i are chosen to be local and δ-like RBFs.

3. It follows that $\hat{T}_p \approx \sum\limits_i f_i\hat{T}_i$, where $\hat{T}_i$ are particular solutions of the inhomogeneous equations

$$\Delta\hat{T}_i + \lambda^2\hat{T}_i = \varphi_i, \quad i = 1,2,...,N_i \tag{17}$$

   Using the space Fourier transform over x, y and the residual technique, closed-form $\hat{T}_i(\mathbf{x},\omega)$ in (17) are derived.

4. The homogenous solution $\hat{T}(h)$ is obtained using the method of fundamental solutions (MFS) [13, 14]; i.e., in terms of fundamental solutions $g(\mathbf{x})$ associated with source points $\mathbf{s}_k$ which are located outside the domain Ω

$$\hat{T}_h(\mathbf{x},\omega) \approx \sum_{k=1}^{N_s} c_k(\omega)g(\mathbf{x}-\mathbf{s}_k). \tag{18}$$

   Unknown coefficients c_k are chosen to satisfy boundary conditions (14) and (15) at collocation points $\mathbf{q}_j \in S, j = 1,2,...,N_s$, allocated on the boundary.

5. For a set of test points $\mathbf{p}_l \in \Omega$, the arrays of spectral values $\hat{T}(\mathbf{p}_l, \omega_m)$, $\omega_m = \omega_{1,m} + i\eta$, $m = 1, ..., M$ are calculated. They are used for the functions $\hat{T}(\mathbf{p}_l, \omega)$ spline approximation on an interval $0 \le \omega_1 \le W$ giving the main contribution into the inverse Fourier integral (8).

6. Finally, time-domain solutions $T(\mathbf{p}_l, t)$ are obtained using the fast Fourier transform (FFT) for the numerical evaluation of the integrals in (8).

3 Derivation of particular solution

In general, a particular solution of any inhomogeneous linear differential equation with constant coefficients may be written as a convolution of its fundamental solution with the forcing term. To derive such a representation for (12), we extend $\hat{f}$ outside Ω by setting it to zero and then apply the Fourier transform over space variables x, y:

$$\tilde{T}_p(\boldsymbol{\alpha}, \omega) = \mathcal{F}_{\mathbf{x}}[\hat{T}_p] = \int_{-\infty}^{\infty}\int_{-\infty}^{\infty} \hat{T}_p(\mathbf{x}, \omega) e^{i<\boldsymbol{\alpha}, \mathbf{x}>} dxdy \tag{19}$$

where $\boldsymbol{\alpha} = (\alpha_1, \alpha_2)$ is the vector of Fourier parameters and $< \boldsymbol{\alpha}, \mathbf{x} >= \alpha_1 x + \alpha_2 y$. The corresponding inverse Fourier transform of $\tilde{T}_p(\boldsymbol{\alpha}, \omega)$ is given by

$$\hat{T}_p(\mathbf{x}, \omega) = \mathcal{F}_{\mathbf{x}}^{-1}[\tilde{T}_p] = \frac{1}{(2\pi)^2}\int_{-\infty}^{\infty}\int_{-\infty}^{\infty} \tilde{T}_p(\boldsymbol{\alpha}, \omega) e^{-i<\boldsymbol{\alpha}, \mathbf{x}>} d\alpha_1 d\alpha_2 \tag{20}$$

Assuming $\hat{T}_p \in C^1(R^2)$, the above Fourier transform further converts (12) to the following form

$$(-\alpha^2 + \lambda^2)\tilde{T}_p(\boldsymbol{\alpha}) = F(\boldsymbol{\alpha}) \tag{21}$$

where $\alpha^2 = |\boldsymbol{\alpha}|^2 = \alpha_1^2 + \alpha_2^2$ and $F(\boldsymbol{\alpha}) = \mathcal{F}_{\mathbf{x}}[\hat{f}(\mathbf{x})]$. From (21), it follows

$$\tilde{T}_p(\boldsymbol{\alpha}) = G(\alpha)F(\boldsymbol{\alpha}) \tag{22}$$

where $G(\alpha) = 1/(-\alpha^2 + \lambda^2)$ is the Fourier symbol of the fundamental solution $g(\mathbf{x})$ for the Helmholtz operator (9). The inverse transformation yields

$$\hat{T}_p(\mathbf{x}) = \frac{1}{(2\pi)^2}\int_{-\infty}^{\infty}\int_{-\infty}^{\infty} G(\alpha)F(\boldsymbol{\alpha}) e^{-i<\boldsymbol{\alpha}, \mathbf{x}>} d\alpha_1 d\alpha_2. \tag{23}$$

Next, substituting

$$F(\boldsymbol{\alpha}) = \iint_{\Omega} \hat{f}(\boldsymbol{\xi}) e^{i<\boldsymbol{\alpha}, \boldsymbol{\xi}>} d\xi_1 d\xi_2, \ \boldsymbol{\xi} = (\xi_1, \xi_2)$$

into (23) and interchanging the order of integrations, we obtain $\hat{T}_p$ as the convolution of g with $\hat{f}$,

$$\hat{T}_p(\mathbf{x}) = (g * \hat{f})(\mathbf{x}) \equiv \iint_{\Omega} g(\mathbf{x} - \boldsymbol{\xi}) \hat{f}(\boldsymbol{\xi}) d\xi_1 d\xi_2, \tag{24}$$

$$g(\mathbf{x}) = \mathcal{F}_{\mathbf{x}}^{-1}[G] = \frac{1}{(2\pi)^2} \int_{-\infty}^{\infty} \int_{-\infty}^{\infty} G(\alpha) e^{-i<\boldsymbol{\alpha},\mathbf{x}>} d\alpha_1 d\alpha_2. \tag{25}$$

As is well-known, $g(\mathbf{x})$ in (25) can be derived analytically in terms of the residue from the pole $\alpha = \lambda$; i.e.,

$$g(\mathbf{x}) = -\frac{i}{4} H_0^{(1)}(\lambda r) \tag{26}$$

where $r = |\mathbf{x}| = \sqrt{x^2 + y^2}$, and $H_0^{(1)}$ is the Hankel function [20].

For simple cases (e.g. $\hat{f} = \text{const}$, Ω is a circle), integrals (23) - (24) can be evaluated analytically. Another way is to use a cubature expansion for (24) in the form

$$\hat{T}_p(\mathbf{x}) \approx h^2 \sum_{i=1}^{N_i} g(\mathbf{x} - \mathbf{x}_i) \hat{f}(\mathbf{x}_i) \tag{27}$$

where $\mathbf{x}_i$ are grid nodes contained in Ω with a spacing h. However, this expansion cannot be used for any $\mathbf{x} \in \Omega$ due to the kernel's logarithmic singularity $g(\mathbf{x}) \sim c \ln |\mathbf{x}| + O(1)$, as $\mathbf{x} \to 0$. To obtain a proper numerical result, this singularity has to be extracted from $g(\mathbf{x} - \boldsymbol{\xi})$ and then integrated explicitly. This task can be achieved if we substitute expansion (16) for $\hat{f}(\mathbf{x})$ in (23) - (24).

In particular, let the basis functions φ_i in (16) be placed at the nodes $\mathbf{x}_i$, $\varphi_i(\mathbf{x}) = \varphi((x - x_i)/h, (y - y_i)/h)$, specified by a radial function $\varphi(x, y) = \varphi(r)$, $r = \sqrt{x^2 + y^2}$. The axial symmetry of φ allows us to gain the most benefit in reducing the four-fold integral (23) to a one-fold form [19, 21]. Indeed, the Fourier transform of a radial function is also axially symmetric with respect to the Fourier parameters α_1, α_2:

$$\begin{aligned} \mathcal{F}_{\mathbf{x}}[\varphi] &= \int_{-\infty}^{\infty} \int_{-\infty}^{\infty} \varphi(r) e^{i<\boldsymbol{\alpha},\mathbf{x}>} dx dy \\ &= \int_0^{\infty} \varphi(r) \int_0^{2\pi} e^{i\alpha r \cos(\gamma - \psi)} d\gamma r dr \\ &= 2\pi \int_0^{\infty} \varphi(r) J_0(\alpha r) r dr \equiv \Phi(\alpha) \end{aligned} \tag{28}$$

In the above derivations we used the change of variables

$$\left\{ \begin{array}{l} x = r\cos\psi \\ y = r\sin\psi \end{array} \right. , \quad \left\{ \begin{array}{l} \alpha_1 = \alpha\cos\gamma \\ \alpha_2 = \alpha\sin\gamma \end{array} \right. , \quad \left\{ \begin{array}{l} r = \sqrt{x^2 + y^2} \\ \alpha = \sqrt{\alpha_1^2 + \alpha_2^2} \end{array} \right. , \tag{29}$$

and the integral representation for the Bessel functions [20, 22]

$$2\pi i^n J_n(\alpha r) = \int_0^{2\pi} e^{i\alpha r\cos(\gamma-\psi)-in\pi} d\gamma. \tag{30}$$

Similarly,

$$\mathcal{F}_{\mathbf{x}}[\varphi_i] = h^2 e^{i<\boldsymbol{\alpha},\mathbf{x}_i>}\Phi(\alpha h) \tag{31}$$

so that in (23)

$$F(\boldsymbol{\alpha}) = \sum_i f_i \mathcal{F}_{\mathbf{x}}[\varphi_i] = h^2\Phi(\alpha h)\sum_i f_i e^{i<\boldsymbol{\alpha},\mathbf{x}_i>}. \tag{32}$$

Since $G(\alpha)\Phi(\alpha h)$ depends only on radial parameter α, we can use the same technique in the inverse Fourier transform again. As a result, we arrive at the following approximation

$$\hat{T}_p(\mathbf{x}) \approx \sum_i f_i\, \hat{T}_i(\mathbf{x}) \tag{33}$$

with

$$\hat{T}_i(\mathbf{x}) = \frac{h^2}{2\pi}\int_0^{\infty} G(\alpha)\Phi(\alpha h) J_0(\alpha r_i)\alpha d\alpha, \tag{34}$$

where $r_i = |\mathbf{x}-\mathbf{x}_i| = \sqrt{(x-x_i)^2+(y-y_i)^2}$. Obviously, $\hat{T}_i(\mathbf{x})$ in (34) are indeed particular solutions of (17), which depend only on radial variables r_i centered at the grid nodes $\mathbf{x}_i$.

Furthermore, if φ_i are compactly supported radial basis functions, which means $\varphi(r) \equiv 0$ for $r \geq h$, a closed form particular solution $\hat{T}_i(\mathbf{x})$ may be derived from (34) for any $r_i \geq h$ (i.e. outside the h-vicinities of the nodes $\mathbf{x}_i$). This can be achieved via unfolding the integration contour from the semi-axis $\alpha \geq 0$ onto the whole real axis $-\infty < \alpha < \infty$ and then closing it in the upper half-plane $\operatorname{Im}\alpha \geq 0$. To unfold the contour, we use the following properties of the Bessel and Hankel functions:

$$J_0(\alpha r_i) = \frac{1}{2}[H_0^{(1)}(\alpha r_i) + H_0^{(2)}(\alpha r_i)],$$
$$H_0^{(2)}(-\alpha r_i) = -H_0^{(1)}(\alpha r_i).$$

This allows us to convert (34) into the form

$$\hat{T}_i(\mathbf{x}) = \frac{h^2}{4\pi}\int_{-\infty}^{\infty} G(\alpha)\Phi(\alpha h) H_0^{(1)}(\alpha r_i)\alpha d\alpha. \tag{35}$$

From the Jordan lemma [23], the integration path may be closed by a semicircle $|\alpha| = R$, $0 \le \gamma \le \pi$ if the integrand tends to zero fast enough as $R \to \infty$. Notice that

$$H_0^{(1)}(\alpha r_i) \sim \text{const} \cdot \frac{e^{i\alpha r_i}}{\sqrt{\alpha r_i}}, \quad |\alpha r_i| \to \infty,$$
$$\Phi(\alpha h) \sim \text{const} \cdot \frac{e^{\pm i\alpha h}}{(\alpha h)^p}, \quad |\alpha h| \to \infty.$$

As a result, the integrand in (35) decreases exponentially in the upper half-plane for $r_i > h$. For such r_i, integral in (35) can be replaced by the residue from the sole pole $\alpha = \lambda$ which is located above the real axis. Then, we have

$$\hat{T}_i(\mathbf{x}) = -\frac{ih^2}{4}\Phi(\lambda h)H_0^{(1)}(\lambda r_i), \quad \text{for} \quad r_i \ge h. \tag{36}$$

The explicit analytic form of $\hat{T}_i(\mathbf{x})$ in (36) is valid for the most part of situations occurred later. A few other integrals such as (34) for $r_i < h$ are to be evaluated via numerical integration. It is not too costly due to integrand's fast decay as $\alpha \to \infty$ even with $r_i = 0$.

We should remark, by this integration in the Fourier transform domain we indirectly integrate the kernel singularity as $r_i \to 0$, which is a special problem for a cubature integration of the convolution integrals (24) in the space domain.

Approximation in (16) in terms of radial functions φ_i is similar to image process using pixel grains in computer graphics or digital photo. Any function $\hat{f}(\mathbf{x})$ given in an arbitrarily shaped domain can be approximated with a reasonable accuracy if a set of nodes $\mathbf{x}_i$ is sufficiently dense. In doing so, the increase of node's number N_i does not necessary lead to high computational cost. This is due to the fact that the overwhelming majority of elements $\hat{T}_i(\mathbf{x})$ forming particular solution $\hat{T}_p(\mathbf{x})$ are evaluated analytically as shown in (36). Since $\hat{T}_i(\mathbf{x})$ depend only on r_i, all of them may be expressed through only one shape function $P(r)$ centered at the corresponding nodes $\mathbf{x}_i$: $\hat{T}_i(\mathbf{x}) = P(r_i)$. A tabulation and proper approximation of this function allows one to avoid recalculation of integrals (34) and Hankel functions in (36).

The approximation of $\hat{T}_p(\mathbf{x})$ in (33) is governed by the coefficients f_i, which play a similar role of pixel's brightness in computer graphics. In general, these coefficients can be obtained using the least square minimization or other related algorithms. However,

with a large number of elements this procedure could be very time-consuming. Therefore, in line with the main idea of [19], we propose a cost effective way for obtaining f_i which is based on the use of so-called δ-like basis functions as follows:

$$\varphi_i(\mathbf{x}) = \varphi\left(\frac{\mathbf{x}-\mathbf{x}_i}{h}\right) \to h^2\delta(\mathbf{x}-\mathbf{x}_i) \quad \text{as} \quad h \to 0. \tag{37}$$

This property holds if

$$\int_{-\infty}^{\infty}\int_{-\infty}^{\infty} \varphi(\mathbf{x})dxdy = 1 \quad \text{and} \quad \varphi(0) \neq 0.$$

In the Fourier transform domain, this is equivalent to the requirements $\Phi(0) = 1$, assuring the asymptotic behavior

$$\Phi_i(\alpha) = h^2\Phi(\alpha h)e^{i<\boldsymbol{\alpha},\mathbf{x}_i>} \sim h^2\, e^{i<\boldsymbol{\alpha},\mathbf{x}_i>} \quad \text{as} \quad h \to 0. \tag{38}$$

A δ-like basis ensures the convergence $f_i \to \hat{f}(\mathbf{x}_i)$ as $h \to 0$ for the coefficients f_i found via minimization of the discrepancy norm $||\hat{f} - \sum f_i\varphi_i||_{L_2}$ [21]. Thus, with such a basis it is sufficient to fix $f_i = \hat{f}(\mathbf{x}_i)$. In this way, the cost of obtaining f_i remains negligible with any N_i, especially in practice $\hat{f}(\mathbf{x})$ may be merely given as an array of experimental data on a set of points.

In particular, one can take the bell-shaped function as a δ-like shape function such as

$$\varphi(\mathbf{x}) = \begin{cases} \dfrac{p+1}{\pi}(1-r^2)^p, & r \leq 1, \\ 0, & r \geq 1. \end{cases} \tag{39}$$

The corresponding Fourier symbol of $\varphi(\mathbf{x})$ is

$$\Phi(\alpha) = \frac{2^{p+1}\Gamma(p+2)J_{p+1}(\alpha)}{\alpha^{p+1}} \tag{40}$$

where $\Gamma(p+2)$ and $J_{p+1}(\alpha)$ are Gamma and Bessel functions.

The form of the shape function $\Phi(\alpha)$ depends on the power exponent p. In principle, by tuning p one can achieve some optimal approximating properties of these basis functions. However, numerical tests show there are little difference for a wide range of p. A convenient choice of p is $\pi - 1$ since $\varphi(0) = 1$. In this case, $\varphi_i(\mathbf{x}_j) = \delta_{ij}$, where δ_{ij} is Kronecker's delta, and expansion (16) with coefficients $f_i = \hat{f}(\mathbf{x}_i)$ provides in addition the exact coincidence in the grid nodes $\mathbf{x}_j$; i.e., $\sum\limits_i f_i\varphi_i(\mathbf{x}_j) = \hat{f}(\mathbf{x}_j)$.

It is worthy to note that expansion (16) with δ-like basis functions leads to a cubature approximation of $F(\alpha)$

$$F(\boldsymbol{\alpha}) = \iint_{\Omega} \hat{f}(\mathbf{x}) e^{i<\boldsymbol{\alpha},\mathbf{x}>} d\mathbf{x} \approx h^2 \sum_i \hat{f}(\mathbf{x}_i) e^{i<\boldsymbol{\alpha},\mathbf{x}_i>}, \quad \text{as} \quad \alpha h \to 0. \tag{41}$$

This is evident from comparison (41) and (32) taking into account (38).

4 Homogeneous solution

After obtaining a particular solution $\hat{T}_p(\mathbf{x},\omega)$, the homogeneous solution $\hat{T}_h(\mathbf{x},\omega)$ is determined by the method of fundamental solutions (MFS) [13, 14]. Based on the formulation of the MFS, $\hat{T}_h$ can be written as the linear combination of the fundamental solutions $g(\mathbf{x}-\mathbf{s}_k)$ centered in source-points $\mathbf{s}_k$ which are located outside of the domain Ω (see (18) and Fig. 1).

Since $\mathbf{s}_k$ are located outside of Ω, this expansion identically satisfies the homogeneous equation (13), while the boundary conditions (14) and (15) are to be satisfied by a proper choice of unknown coefficients $\{c_k\}_{k=1}^{N_s}$ in (18). This can be achieved using different variational approaches such as Galerkin or Petrov-Galerkin discretization schemes. The most simple in implementation, however, is the collocation method. It is quite applicable here since we do not expect oscillation of the solution among the collocation points as often takes place in wave problems. Due to a high attenuation ($\mathrm{Im}\,\lambda = \mathrm{Re}\lambda$), a temperature field governed by (9) normally exhibits a very smooth variation in space and frequency domains. Hence, by substituting (18) into boundary conditions (14) and (15) at $N_s = N_D + N_N$ collocation points $\{\mathbf{q}_j\} \in S$, we have

$$\mathbf{G}\mathbf{c} = \mathbf{b}$$

where $\mathbf{G} = [G_{jk}], \mathbf{b} = [b_j], \mathbf{c} = [c_j]$ with

$$G_{jk} = \begin{cases} g(\mathbf{q}_j - \mathbf{s}_k), & j = 1, ..., N_D, \\ \dfrac{\partial g(\mathbf{q}_j - \mathbf{s}_k)}{\partial n_j}, & j = N_D + 1, ..., N_s, \end{cases} \tag{42}$$

$$b_j = \begin{cases} \hat{T}_D(\mathbf{q}_j) - \hat{T}_p(\mathbf{q}_j), & j = 1, ..., N_D, \\ \hat{T}_N(\mathbf{q}_j) - \dfrac{\partial \hat{T}_p(\mathbf{q}_j)}{\partial n_j}, & j = N_D + 1, ..., N_s, \end{cases} \tag{43}$$

and N_D is the number of collocation points on S_D, $\partial/\partial n_j = \nabla \cdot \mathbf{n}_j$ are normal to S derivatives in the points $\mathbf{q}_j \in S_N$, $\mathbf{n}_j$ are unit outward normals at these points. The derivatives act on the Hankel function $H_0^{(1)}(\lambda r)$ entering in $g(\mathbf{x})$ and on the particular solution $\hat{T}_p$. In view of the properties

$$J_0^{'}(x) = -J_1(x) \quad \text{and} \quad [H_0^{(1)}(x)]^{'} = -H_1^{(1)}(x),$$

we arrive at the following representations

$$\frac{\partial g(\mathbf{q}_j - \mathbf{s}_k)}{\partial n_j} = \frac{i\lambda}{4} H_1^{(1)}(\lambda r_{jk}) \frac{\mathbf{n}_j \mathbf{r}_{jk}}{r_{jk}},$$
$$\frac{\partial \hat{T}_p(\mathbf{q}_j)}{\partial n_j} = \sum_i f_i \frac{\partial \hat{T}_i(\mathbf{q}_j)}{\partial n_j},$$

$$\frac{\partial \hat{T}_i(\mathbf{q}_j)}{\partial n_j} = \frac{\mathbf{n}_j \boldsymbol{\rho}_{ji}}{\rho_{ji}} h^2 \begin{cases} \dfrac{i\lambda}{4} \Phi(\lambda h) H_1^{(1)}(\lambda \rho_{ji}), & \rho_{ji} > h, \\ \\ -\dfrac{1}{2\pi} \displaystyle\int_0^\infty G(\alpha) \Phi(\alpha h) J_1(\alpha \rho_{ji}) \alpha^2 d\alpha, & \rho_{ji} \le h, \end{cases}$$

$$\mathbf{r}_{jk} = \mathbf{q}_j - \mathbf{s}_k, \quad r_{jk} = |\mathbf{r}_{jk}|$$
$$\boldsymbol{\rho}_{ji} = \mathbf{q}_j - \mathbf{x}_i, \quad \rho_{ji} = |\boldsymbol{\rho}_{ji}|.$$

5 Numerical results in the frequency domain

To estimate the working capacity and accuracy of the scheme described above, a systematic comparison with the exact solution has been carried out. The test problem is taken from the example in [24]. It is the rectangular domain Ω: $|x| \le a$, $|y| \le b$ with $a = b = 0.1$ m, the material density $\rho = 80$ kg/m^3, the thermal conductivity $k = 0.06$ $W/m\,C^o$ and the thermal coefficient $c = 1300$ $J/kg\,C^o$. There is no heat source ($f \equiv 0$) and the boundary conditions are kept at zero temperature (homogeneous Dirichlet conditions $T|_S = 0$). Unlike [24], however, the initial temperature distribution is taken to be non-constant:

$$T_0(\mathbf{x}) = \cos \frac{\pi}{2a} x \cos \frac{\pi}{2b} y \tag{44}$$

which assumes non-trivial approximation for the particular solution, so that the expression (33) is used in essence.

The exact solution is given as follows:

$$T(\mathbf{x},t) = T_0(\mathbf{x})e^{-dt}, \quad d = K\left(\frac{\pi}{2}\right)^2\left(\frac{1}{a^2}+\frac{1}{b^2}\right). \tag{45}$$

Its Fourier spectrum is

$$\hat{T}(\mathbf{x},\omega) = \frac{T_0(\mathbf{x})}{d-i\omega}. \tag{46}$$

For the rest of this example, we use dimensionless parameters with the following set of units:

$l_0 = 1\ m$ as the unit of length,

$t_0 = 10^3\ s$ as the unit of time, $\omega_0 = 2\pi \cdot 10^{-3}\ s^{-1}$ as the unit of frequency,

$C_0 = 1\ C^o$ as the unit of temperature.

In these units, $a = b = 0.1$, the thermal diffusivity $K = 0.00058$ and d in (45) is equal to 0.2862. In all the following numerical examples, the source points $\mathbf{s}_k$ are placed at the equal distance from S: $d_k = a$.

Numerical tests have exhibited good agreement between the approximate solution $\hat{T}_N = \hat{T}_p + \hat{T}_h$ and the exact solution $\hat{T}$ in (46) while using a moderate number of source points $\{\mathbf{s}_k\}, i = 1, ..., N_s$, and a rather coarse grid for the approximation of $\hat{T}_p$. With a higher values N_s and $N_i = N_x \cdot N_y$, which affect the accuracy of $\hat{T}_h$ and $\hat{T}_p$ respectively, the difference between the numerical and analytical solutions becomes practically indistinguishable on the plots versus both space and spectral variables $\mathbf{x}$ and ω as shown in Fig. 2. The solid curves show the analytical solution $|\hat{T}|$ versus ω at three fixed test points $\mathbf{x} = \mathbf{p}_l$: $\mathbf{p}_1 = (0,0)$, $\mathbf{p}_2 = (a/3, 0)$ and $\mathbf{p}_3 = (2a/3, 0)$ (top-down), while the circles denote the values $|\hat{T}_N(\mathbf{p}_l, \omega_m)|$ obtained numerically using $N_s = 40$, $N_x = N_y = 100$.

The overall accuracy can be evaluated in terms of the integral relative error

$$E_r = \left| \frac{\iint_\Omega \left(\hat{T} - \hat{T}_N\right) d\mathbf{x}}{\iint_\Omega \hat{T} d\mathbf{x}} \right| \tag{47}$$

where $\hat{T}$ is explicit solution and $\hat{T}_N$ is numerical solution. Table 1 shows the E_r using various N_s and $N_x = N_y$ at a fixed ω.

To calculate E_r, the integrals in (47) are approximated by a cubature sum over an evenly distributed testing points $\mathbf{p}_l$. For comparability, we took the same grid 20×20 with various N_s and N_x.

Since $\hat{T}_N$ is the sum of $\hat{T}_p$ and $\hat{T}_h$, the total accuracy E_r could not be better than the lesser accuracy of each of them. Hence, increasing N_s with a fixed N_x will not improve the accuracy after a certain point at which $\hat{T}_h$ error becomes less than the error of $\hat{T}_p$. Similarly, N_x (or generally, $N_i = N_x \cdot N_y$) should not be taken over a certain value, which is specific for each given set of source points $\mathbf{s}_k$ forming $\hat{T}_h$. These limiting values can be observed in Table 1. For instance, along the table rows the E_r continue to improve until $N_x = 50$ for $N_s = 16$; $N_x = 200$ for $N_s = 20$; $N_x = 400$ for $N_s = 24$, etc. If we observe from column, E_r becomes stable after the row $N_s = 32$. This means the particular solution $\hat{T}_p$ plays a major role for the total accuracy E_r for $N_s > 32$. With a finer grid $\mathbf{x}_i$ (that is, with $N_x > 400$) this threshold number of the fundamental solutions used for $\hat{T}_h$ approximation also increases which will provide further improvement for E_r.

As for a time-domain solution, its accuracy also depends on the accuracy of numerical evaluation of the inverse Fourier integrals (8).

6 Solution in the time domain

After the evaluation of $\hat{T}_p(\mathbf{x}, \omega)$ in (33) and $\hat{T}_h(\mathbf{x}, \omega)$ in (18) for a set of spectral parameters $\omega_m = \omega_{1,m} + i\eta, m = 1, 2, ..., M$, we proceed to calculate the temperature field $T(\mathbf{x}, t)$ using numerical integration for the inverse Fourier integral (8). A simple and direct way to approximate it is by the quadrature rule as follows:

$$T(\mathbf{x}, t) \approx \frac{1}{\pi} \operatorname{Re} \sum_{m=1}^{M} \hat{T}(\mathbf{x}, \omega_m) e^{-i\omega_m t} \Delta_m \tag{48}$$

where Δ_m are quadrature coefficients, e.g. lengths of bases in the rectangular formula. However, due to oscillation $e^{-i\omega t}$ this approximation is very sensitive to the value of time t. To keep the required accuracy as t grows, the number of nodes M may increase so dramatically that the calculation of $\hat{T}(\mathbf{x}, \omega)$ for each ω_m becomes very time consuming.

On the other hand, spectrum $\hat{T}(\mathbf{x}, \omega)$ does not depend of t, hence nodes ω_m may be fixed disregarding t. The computed values $\hat{T}(\mathbf{x}, \omega_m)$ are then used to approximate $\hat{T}(\mathbf{x}, \omega)$ in a spectrum interval $0 \leq \operatorname{Re} \omega \leq W$ where upper limit W is determined by the rate of spectrum decay as $\operatorname{Re} \omega \to \infty$. In our calculation, we use Akima's spline interpolation [25] to prevent a superfluous spline winding. As soon as $\hat{T}(\mathbf{x}, \omega)$ is properly interpolated, we can use any number of nodes ω_k for the numerical integration without considerable

computational cost. The best way is to choose ω_k so that to get a discrete fast Fourier transform (FFT) representation. In this way, $T(\mathbf{x},t)$ in N time-points t_n are obtained simultaneously through the values of the integrand in N nodes ω_k.

Indeed, let us consider the discrete Fourier transform pair

$$\begin{cases} X(n) = \sum_{k=1}^{N} Y(k) e^{-i2\pi(k-1)(n-1)/N}, \quad n = 1, 2, ..., N, \\ Y(k) = \sum_{n=1}^{N} X(n) e^{i2\pi(k-1)(n-1)/N}, \quad k = 1, 2, ..., N. \end{cases} \tag{49}$$

Since FFT provides very fast X output in response to an input array Y, our primary goal is to bring (48) to the form (49). For this purpose, let us denote

$$\bar{\omega}_{1,k} = 2\pi(k-1), \quad \bar{t}_n = \frac{(n-1)}{N}, \quad X(n) = \bar{T}_n, \quad Y(k) = \hat{T}_k.$$

The first sum in (49) takes the form

$$\bar{T}_n = \sum_{k=1}^{N} \hat{T}_k e^{-i\bar{\omega}_{1,k}\bar{t}_n} \tag{50}$$

The normalized time-points $\bar{t}_n$ lie in the unit interval $0 \leq \bar{t}_n < 1$. Therefore, to get the result in the time-points $t_n \in [0, \tau]$, it is necessary to re-scale it through the change of variables

$$t = \tau\bar{t}, \quad \omega = \frac{\bar{\omega}}{\tau}. \tag{51}$$

From (8),

$$\begin{aligned} T_n(\mathbf{x}) = T(\mathbf{x}, t_n) &= \frac{1}{\pi\tau} \operatorname{Re} \int_0^\infty \hat{T}\left(\mathbf{x}, \frac{\bar{\omega}}{\tau}\right) e^{-i\bar{\omega}\bar{t}_n} d\bar{\omega}_1 \\ &\approx \frac{1}{\pi\tau} \operatorname{Re} \sum_{k=1}^{N} \hat{T}_k e^{-i\bar{\omega}_{1,k}\bar{t}_n} e^{\eta t_n} \Delta\bar{\omega} \end{aligned} \tag{52}$$

where

$$\hat{T}_k = \hat{T}\left(\mathbf{x}, \frac{\bar{\omega}_k}{\tau}\right), \quad \omega_k = \frac{\bar{\omega}_{1,k}}{\tau} + i\eta, \quad \Delta\bar{\omega} = \bar{\omega}_{1,k+1} - \bar{\omega}_{1,k} = 2\pi.$$

Therefore, within the accuracy of the integral (8) approximation by the sum (52), we take

$$T_n = \frac{2}{\tau} e^{\eta t_n} \operatorname{Re} \bar{T}_n \tag{53}$$

where constants $\bar{T}_n$ are provided by an FFT code on the input $\hat{T}_k$ array in accordance with (50).

It should be noted once again, as soon as $\hat{T}(\mathbf{x},\omega)$ is properly approximated, there are practically no restriction in choosing the number of points N to reach the required accuracy in the approximation of $T_n(\mathbf{x})$ in (52). It depends on the integration step $\Delta\omega = \Delta\bar{\omega}/\tau = 2\pi/\tau$, which is the smaller for the larger time interval τ. Hence, τ should be taken as large as possible, even if it is required to get results on a limited time interval $\tau_1 \le t \le \tau_2$. However, the time-points t_n, in which FFT yields $\bar{T}_n$, cover the interval $0 \le t \le \tau$ with the step $\Delta t = \tau/N$ in which $t_n = (n-1)\cdot\Delta t$. With a fixed N, therefore, τ should not be too large to provide enough points t_n on $[\tau_1, \tau_2]$.

Generally, N and τ are not independent because the number of spectral points ω_k should be enough to cover the entire interval of numerical integration $0 \le \omega \le W$ with the spacing $\Delta\omega$. This puts the limitation $\omega_N = N\cdot 2\pi/\tau \ge W$ (or $\tau \le 2\pi N/W$).

A proper choice of these parameters (τ and N) for a given well-approximated $\hat{T}(\mathbf{x},\omega)$ over ω spectrum provides reasonable accuracy in the time-domain. In Fig. 3, $T_n(\mathbf{p}_l)$ (circles) obtained by (53) are plotted together with the exact solution (45) (solid lines). The test points $\mathbf{p}_l$ and the spectral functions $\hat{T}(\mathbf{p}_l,\omega)$ are the same as in Fig. 2. For the FFT application they were computed in the spectral range $0 \le \omega \le 40$ with the step $\Delta\omega_m = 0.1$ ($M = 400$), and then approximated by splines. The results in time-domain are obtained using $\tau = 1000$ and $N = 6400$ which takes less than one second in a 1.3 GHz PC. Since $T(\mathbf{x},t)$ is discontinuous at $t = 0$ ($T \equiv 0$ for $t < 0$), the inverse Fourier transform (7) yields

$$T(\mathbf{x},0^+) = \frac{1}{2}\lim_{t\to 0^+} T(\mathbf{x},t).$$

That is why the circles at $t = 0$ in Fig. 3 lie at about a half height of the corresponding analytical values.

In Fig. 5, we show a temperature-time plot at the points $\mathbf{p}_l$ but resulted from the local initial temperature loading

$$T_0(x,y) = \begin{cases} \cos\left(\dfrac{\pi r}{2r_0}\right), & r \le r_0, \\ 0, & r > r_0, \end{cases} \tag{54}$$

where $r = \sqrt{(x-x_0)^2 + (y-y_0)^2}$, $x_0 = -a/2$, $y_0 = a/2$, $r_0 = a/3$. This temperature field is shown in Fig. 4 by a grey scale; points $\mathbf{p}_l$ are marked by dots on the x-axis.

The main special feature of this example is that for a localized initial field T_0 the points lying out of the heated area keep zero temperature until the heat-diffusion flow has

reached them. After this, the point is getting warm up to a certain maximal temperature and then, after the maximal heat has passed by, it becomes cooling down. The plots in Fig. 5 show such behavior. They were calculated using the following input parameters: $W = 40$, $M = 400$, $\tau = 10000$, $N = 64000$.

7 Conclusion

In this paper we propose a meshless and semi-analytical method for the numerical simulation of general heat transfer problem with nonzero initial condition in a 2D domain. The method involves Fourier transforms in time and space domains, and expansions in terms of classical fundamental and elementary radial partial solutions. A semi-analytical particular solution using expansion in term of δ-like basis function has been derived which is one of the main focus of this paper. For the homogeneous solution, the standard MFS has been employed. We also applied the fast Fourier transform to convert the solution in the frequency domain to time domain. Numerical tests confirm the applicability of the proposed approach to a wide class of heat-transfer problems.

The proposed approach provides an alternative for solving heat transfer problems. It can be also extended to the numerical simulation of wave equations, convection-diffusion equations, and other nonhomogeneous time-dependent problems.

Acknowledgement

The work is supported by the NATO Collaborative Linkage Grant PST.CLG.980398 and by the Russian Foundation for Basic Research (grant No 04-01-00801).

References

[1] G.L. Moridis and D.L. Reddell, The Laplace Transform Boundary Element (LTBE) Method for the Solution of Diffusion-Type Equations, *Boundary Elements XIII*, vol. 1, pp. 83-97, Springer-Verlag, Berlin, 1991.

[2] C.K. Chen, T.M. Chen, and J.W. Cleaver, New Hybrid Laplace Transform/Finite Element Method for Two-Dimensional Transient Heat Conduction Problem, *Numer. Heat Transfer B*, vol. 20, pp. 191-205, 1991.

[3] S. Zhu, P. Satravaha, and X. Lu, Solving Linear Diffusion Equations with the Dual Reciprocity Method in Laplace Space, *Engng. Anal. Boundary Elem.*, vol. 13, pp. 1-10, 1994.

[4] C.S. Chen, M.A. Golberg and Y.F. Rashed, A Mesh Free Method for Linear Diffusion Equations, *Numer. Heat Transfer B*, vol. 33, pp. 469-486, 1998.

[5] M.A. Golberg and C.S. Chen, A Mesh Free Method for Solving Nonlinear Reaction-Diffusion Equations, *the Journal of Computer Modeling in Engineering & Science*, vol. 2, pp. 87-95, 2001.

[6] M.S. Ingber, C.S. Chen, and J.A. Tanski, A Mesh Free Approach Using Radial Basis Functions and Parallel Domain Decomposition for Solving Three Dimensional Diffusion Equations, *International Journal of Numerical Methods in Engineering*, vol. 60, pp. 2183-2201, 2004.

[7] X. Li and C.S. Chen, A Mesh-Free Method Using Hyperinterpolation and Fast Fourier Transform for Solving Differential Equation, *Eng. Analysis with Boundary Elements*, vol. 28, pp. 1253-1260, 2004.

[8] Y. Liu, X. Zhang, and M. W. Lu, A Meshless Method Based on Least Squares Approach for Steady- and Unsteady-State Heat Conduction Problems, *Numer. Heat Transfer B*, vol. 47, pp. 257-275, 2005.

[9] H. Sadat, N. Dubus, L. Gbahoué and T. Sophy, On the solution of heterogeneous heat conduction problems by a diffuse approximation meshless method, Numerical Heat Transfer, Part B, 50(6), pp. 491-498, 2006.

[10] R.M. Cotta and J.E.V. Gerk, Mixed Finite-Difference/Integral Transform Approach for Parabolic-Hyperbolic Problems in Transient Forced Convection, *Numer. Heat Transfer B*, vol. 25, pp. 433-448, 1994.

[11] Der-Liang Young, Chia-Cheng Tsai, and Chia-Ming Fan, Direct Approach to Solve Nonhomogeneous Diffusion Problems Using Fundamental Solutions and Dual Reciprocity Methods, *Journal of the Chinese Institute of Engineers*, vol. 27, pp. 597-609, 2004.

[12] H. Cho, M.A. Golberg, A.S. Muleshkov, and X. Li, Trefftz Methods for Time Dependent Partial Differential Equations, *CMC*, vol. 1, pp. 1-37, 2004.

[13] G. Fairweather and A. Karageorghis, The Method of Fundamental Solution for Elliptic Boundary Value Problems, *Advances in Computatonal Mathematics*, 9, pp. 69-95, 1998.

[14] M.A. Golberg, and C.S. Chen, The Method of Fundamental Solutions for Potential, Helmholtz and Diffusion Problems, in M.A. Golberg (ed.), *Boundary Integral Methods - Numerical and Mathematical Aspects*, Computational Mechanics Publications, Southampton, pp. 103-176, 1998.

[15] K.E. Atkinson, The Numerical Evaluation of Particular Solutions for Poisson's Equation, *IMA J. Numer. Anal.*, vol. 5, pp. 319-338, 1985.

[16] A.S. Muleshkov, M.A. Golberg, and C.S. Chen, Particular Solutions of Helmholtz-Type Operators Using Higher Order Polyharmonic Splines, *Computational Mechanics*, vol. 23, pp. 411-419, 1999.

[17] C.S. Chen, M.A. Golberg, and R.S. Schaback, Recent Developments of the Dual Reciprocity Method Using Compactly Supported Radial Basis Functions, in Y.F. Rashed (ed.), *Transformation of Domain Effects to the Boundary*, WIT Press, Southampton, pp. 183-225, 2003.

[18] P.W. Partridge, C.A. Brebbia, L.C. Wrobel, *The Dual Reciprocity Boundary Element Method*, Computational Mechanics Publications, Southampton, Boston, 1992.

[19] E. Glushkov and N. Glushkova, On the Efficient Implementation of the Integral Equation Method in Elastodynamics, *Journal of Computational Acoustics*, vol. 9, pp. 889-898, 2001.

[20] M. Abramowitz and I.A. Stegun (eds.), *Handbook of Mathematical Functions. Applied Mathematics Series 55*, National Bureau of Standards, Washington D.C., 1964.

[21] V.A. Babeshko, E.V. Glushkov, and J.F. Zinchenko, *Dynamics of Inhomogeneous Linearly Elastic Media*, Nauka, Moscow, pp. 1-344, 1989 (in Russian).

[22] H. Bateman and A. Erdelyi, *Higher Transcendental Functions*, Vol. 2, McGraw-Hill book company, Inc., New-York, Toronto, London, 1953.

[23] J.E. Marsden, *Basic Complex Analysis*, W.H. Freeman and Company, 1973.

[24] A. Tadeu, C.S. Chen, J. Antonio, and Nuno Simoes, Conduction Heat Transfer under Nonzero Initial Conditions: A Solution Using the Method of Particular Solutions in the Frequency Domain, (submitted for publication).

[25] H. Akima, A New Method of Interpolation and Smooth Curve Fitting Based on Local Procedures, *Journal of ACM*, vol. 17, pp. 589-602, 1970.

Table 1: Relative accuracy E_r at $\omega = 0.5$.

$N_s \setminus N_x$	25	50	100	200	400
16	0.004289	0.001439	0.002806	0.003149	0.003238
20	0.007345	0.001739	0.000354	0.000148	0.000194
24	0.007623	0.002019	0.000599	0.000255	0.000163
28	0.007505	0.001908	0.000489	0.000144	0.000052
32	0.007476	0.001888	0.000468	0.000124	0.000031
40	0.007483	0.001890	0.000468	0.000124	0.000031
100	0.007497	0.001886	0.000468	0.000123	0.000031

Figure captions

Fig1: Nodes $\mathbf{x}_i$, source points $\mathbf{s}_k$, collocation points $\mathbf{q}_j$, and test points $\mathbf{p}_l$.

Fig2: Exact and approximate temperature fields at three test points in the frequency domain.

Fig3: Exact and approximate temperature fields at three test points in time-domain.

Fig4: Initial temperature field and reference points.

Fig5: Time-domain solution at the reference points.

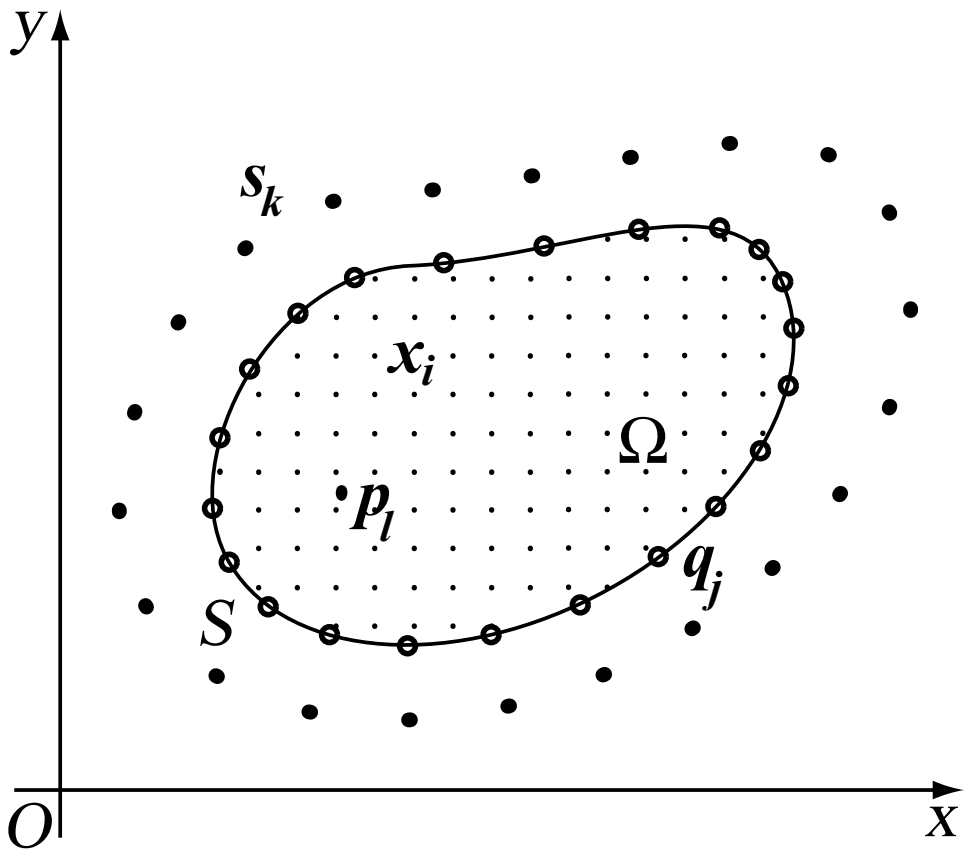

Figure 1: Nodes $\mathbf{x}_i$, source points $\mathbf{s}_k$, collocation points $\mathbf{q}_j$, and test points $\mathbf{p}_l$.

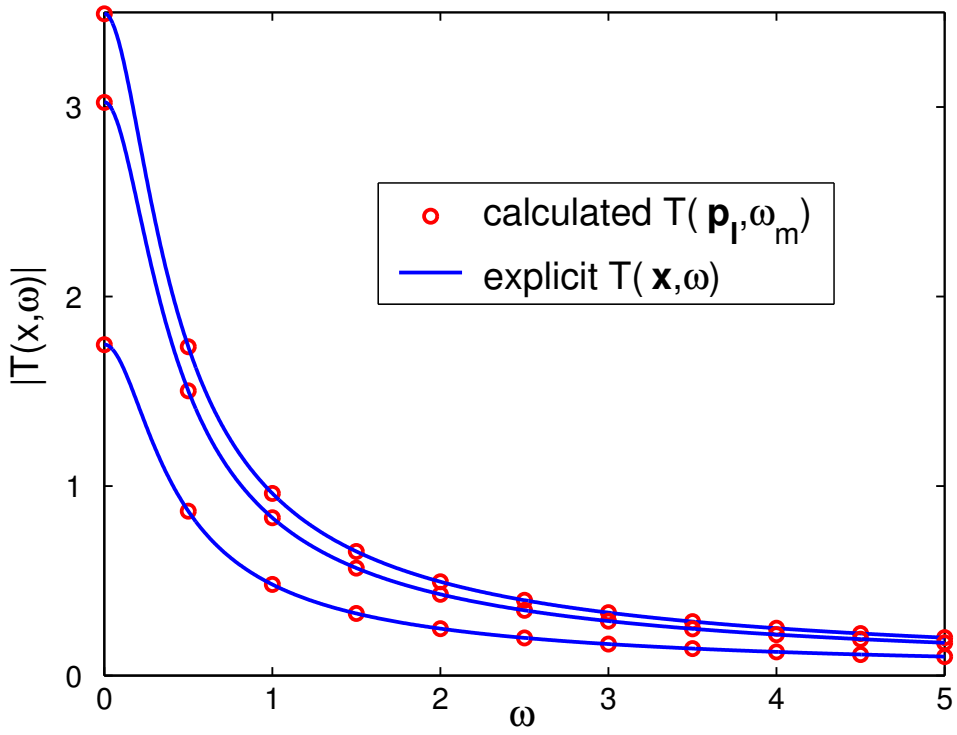

Figure 2: Exact and approximate temperature fields at three test points in the frequency domain.

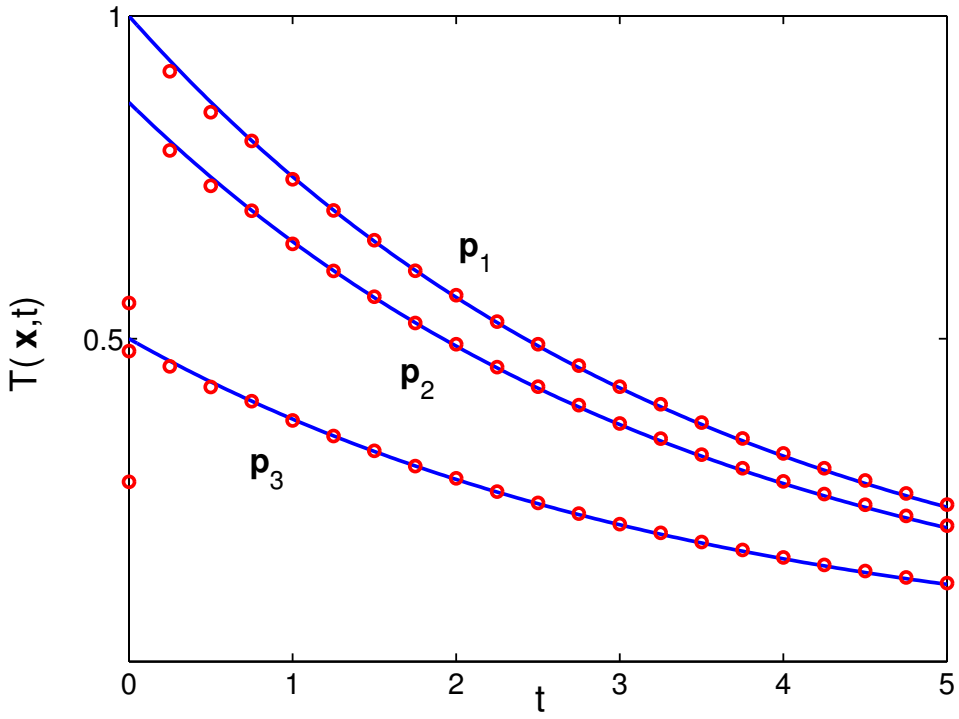

Figure 3: Exact and approximate temperature fields at three test points in time-domain.

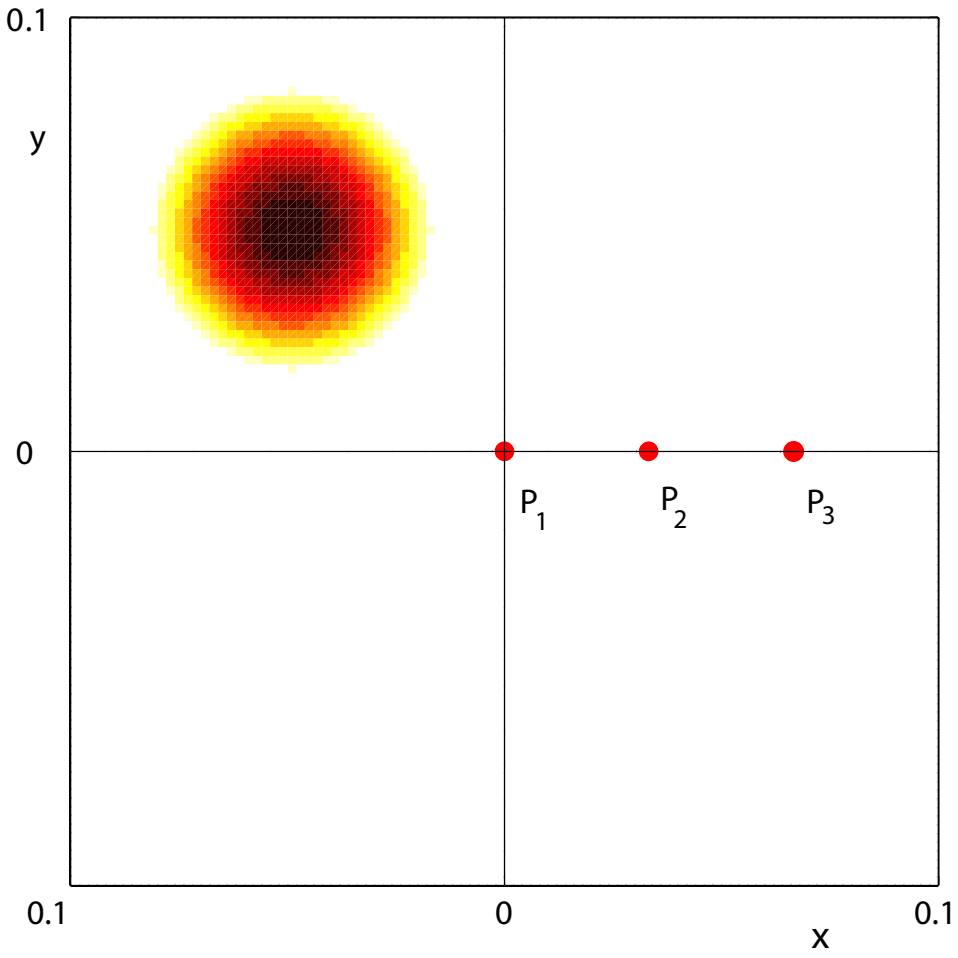

Figure 4: Initial temperature field and reference points

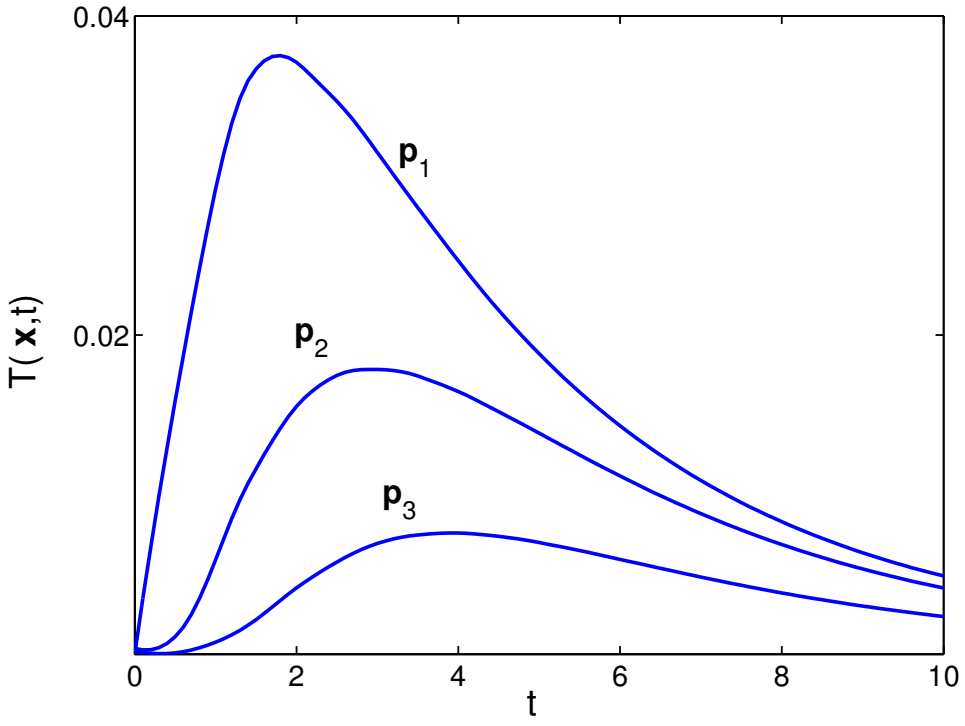

Figure 5: Time-domain solution at the reference points